nature materials

ARTICLES

https://doi.org/10.1038/s41563-020-0652-5

Nonlinear Luttinger liquid plasmons in semiconducting single-walled carbon nanotubes

Sheng Wang[1,2], Sihan Zhao[1], Zhiwen Shi[3,4], Fanqi Wu[5], Zhiyuan Zhao[5], Lili Jiang[1], Kenji Watanabe[6], Takashi Taniguchi[6], Alex Zettl[1,2,7], Chongwu Zhou[5,8] and Feng Wang[1,2,7] ✉

Interacting electrons confined in one dimension are generally described by the Luttinger liquid formalism, where the low-energy electronic dispersion is assumed to be linear and the resulting plasmonic excitations are non-interacting. Instead, a Luttinger liquid in one-dimensional materials with nonlinear electronic bands is expected to show strong plasmon–plasmon interactions, but an experimental demonstration of this behaviour has been lacking. Here, we combine infrared nano-imaging and electronic transport to investigate the behaviour of plasmonic excitations in semiconducting single-walled carbon nanotubes with carrier density controlled by electrostatic gating. We show that both the propagation velocity and the dynamic damping of plasmons can be tuned continuously, which is well captured by the nonlinear Luttinger liquid theory. These results contrast with the gate-independent plasmons observed in metallic nanotubes, as expected for a linear Luttinger liquid. Our findings provide an experimental demonstration of one-dimensional electron dynamics beyond the conventional linear Luttinger liquid paradigm and are important for understanding excited-state properties in one dimension.

Electrons in three- and two-dimensional metals are well represented by weakly interacting quasi-particles within Fermi liquid theory. However, this theory breaks down in one dimension, where Coulomb interactions become dominant and can qualitatively alter the electronic behaviours. Luttinger liquid theory, which is based on the linearization of the dispersion relation of the particles constituting the fluid, can successfully describe many exotic phenomena in one-dimensional (1D) metals such as spin–charge separation and the power-law dependence of spectral functions near the Fermi level[1–14]. However, the electronic band dispersion in real 1D systems is often not strictly linear, and the linearization taken in Luttinger liquid theory limits its validity to low-energy electron behaviours. To describe high-energy quasi-particle excitations and dynamics, more general theoretical approaches have been employed to replace the linear dispersion with a generic one, which is known as nonlinear Luttinger liquid theory[15–22]. This nonlinear theory predicts many intriguing electron behaviours beyond the linear Luttinger liquid paradigm. For instance, the collective electron excitations (that is, plasmons) in a linear Luttinger liquid are expected to be extremely long-lived due to the absence of an intrinsic relaxation mechanism. However, in a nonlinear Luttinger liquid, the nonlinearity of the band dispersion can strongly mix different plasmon excitations, resulting in a drastic reduction of plasmon lifetime. Such unusual excited-state dynamics of a nonlinear Luttinger liquid have rarely been experimentally explored previously.

Here we probe nonlinear Luttinger liquid physics using gated semiconducting carbon single-walled nanotubes (SWNTs) as a model system and compare the behaviour to that of a linear Luttinger liquid in metallic SWNTs. We systematically vary the carrier density in metallic and semiconducting nanotubes through electrostatic gating while performing in situ infrared nano-imaging as schematically shown in Fig. 1a. We show that the plasmon wavelength, amplitude and quality factor in semiconducting SWNTs can be continuously tuned due to the nonlinear band dispersion. In particular, our results reveal the unusual relaxation dynamics of plasmon excitations in semiconducting SWNTs as described by nonlinear Luttinger liquid theory, and their behaviours are in marked contrast with those of the linear Luttinger liquid plasmon excitations present in metallic SWNTs.

Metallic and semiconducting SWNTs are directly grown by chemical vapour deposition (CVD) onto hexagonal boron nitride (h-BN) flakes exfoliated on top of a SiO_2/Si substrate (SiO_2, 285 nm; see Methods for details). Atomic force microscopy (AFM) characterization of these SWNTs shows that they are ultraclean and very long, which can be readily integrated into field-effect transistor (FET) devices[23]. We probe the plasmons in gated nanotube devices at different carrier densities using infrared scanning near-field optical microscopy (IR-SNOM) as illustrated in Fig. 1a (refs. [12,23–25]). To achieve infrared nano-imaging by IR-SNOM, AFM operates under a tapping mode, with its gold-coated tip illuminated with an infrared light with wavelength 10.6 μm. The sharp tip acts as an optical nanoantenna that couples the incident light to plasmons in the SWNTs. The launched plasmon wave propagates towards and reflects off the ends of the SWNTs, which results in an interference pattern between the tip-launched plasmon field and the reflected plasmon field. The plasmon field is scattered by the tip to the far field, which is captured by a mercury cadmium telluride (MCT) detector. We visualize the plasmon interference pattern by a raster scanning of the sample.

The electronic band structures of metallic and semiconducting SWNTs are illustrated in Fig. 1b,c, respectively[26]. Metallic nanotubes feature a gapless linear band dispersion, $E = \hbar v_0 k_F$, where $\hbar$

[1]Department of Physics, University of California at Berkeley, Berkeley, CA, USA. [2]Materials Sciences Division, Lawrence Berkeley National Laboratory, Berkeley, CA, USA. [3]Key Laboratory of Artificial Structures and Quantum Control (Ministry of Education), Shenyang National Laboratory for Materials Science, School of Physics and Astronomy, Shanghai Jiao Tong University, Shanghai, China. [4]Collaborative Innovation Center of Advanced Microstructures, Nanjing, China. [5]Department of Chemical Engineering and Materials Science, University of Southern California, Los Angeles, CA, USA. [6]National Institute for Materials Science, Tsukuba, Japan. [7]Kavli Energy NanoScience Institute at the University of California, Berkeley and the Lawrence Berkeley National Laboratory, Berkeley, CA, USA. [8]Department of Electrical Engineering, University of Southern California, Los Angeles, CA, USA. ✉e-mail: fengwang76@berkeley.edu

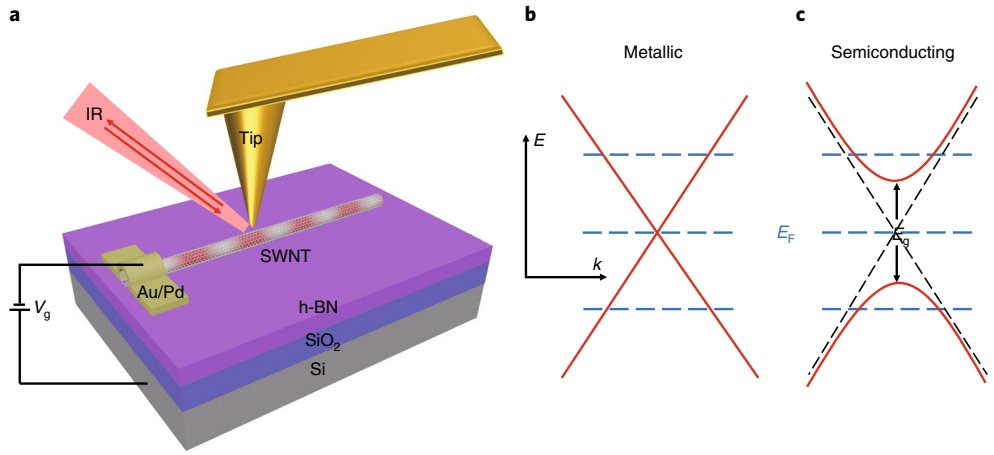

Fig. 1 | Schematic of IR-SNOM of SWNTs with carrier density controlled by electrostatic gating. a, Schematic of infrared nano-imaging of a nanotube FET device. Ultraclean SWNTs are directly grown by CVD onto hexagonal boron nitride (h-BN) flakes exfoliated on top of a SiO_2/Si substrate (SiO_2, 285 nm; see Methods for details). A back-gate voltage V_g is applied between the metal electrode (Au/Pd) contacting the SWNT and the Si substrate to tune the carrier concentration in the SWNT. For infrared (IR) nano-imaging, a gold-coated AFM tip is illuminated with infrared light with wavelength 10.6 μm. The backscattered signal from the tip–sample system carries essential plasmon information of the sample. By a raster scanning of the sample, near-field images are obtained simultaneously with the topography. **b**, Band structure of metallic SWNTs. Metallic SWNTs feature a gapless linear energy–momentum (E–k) dispersion, schematically shown as the red curve. **c**, Band structure of semiconducting SWNTs. Semiconducting SWNTs feature a hyperbolic E–k dispersion (schematically shown as the red curve) with a finite band gap E_g. The diagonal black dashed lines indicate the linear band structure of metallic SWNTs for comparison with the hyperbolic band structure of semiconducting SWNTs. When a back-gate voltage V_g is applied in **a** relative to the charge neutral point V_{cnp}, the Fermi level E_F indicated by the horizontal dashed blue lines in metallic and semiconducting SWNTs can be continuously tuned.

is the reduced Planck's constant, v_0 (~0.8×10^6 m s^{-1}) is the Fermi velocity in graphene and k_F is the Fermi wavevector. Their 1D linear bands provide an ideal realization of the linear Luttinger liquid. Semiconducting nanotubes, by contrast, have a finite band gap E_g and feature a hyperbolic dispersion, $E^2 = (E_g/2)^2 + (\hbar v_0 k_F)^2$, where E_g is inversely proportional to the nanotube diameter d as $E_g = 0.75\,\text{eV}/d$ (where d is in nm). When a back-gate voltage V_g is applied (Fig. 1a) relative to the charge neutral point V_{cnp}, the Fermi level E_F in both metallic and semiconducting SWNTs can be continuously tuned from hole doping to charge neutrality and to electron doping, as illustrated in Fig. 1b,c. The charge neutral point V_{cnp} is the gate voltage needed to offset the unintentional doping, usually coming from the substrate.

In Fig. 2, we present a detailed study of the dependence of plasmon excitations on carrier density in semiconducting SWNTs and compare that with plasmon excitations in doped metallic SWNTs. The carrier type in SWNTs is continuously tuned from hole doping to charge neutrality and then to electron doping as the gate voltage V_g is varied from −20 to 20 V. The near-field images at these different gate voltages are shown in Fig. 2a–f. The topography recorded simultaneously is shown in the top right inset in Fig. 2a. In the near-field images, nanotubes labelled M1 and M2 in Fig. 2a exhibit prominent oscillation peaks at all gate voltages (Fig. 2a–f). These are gapless metallic SWNTs with linear dispersion. The peaks in the near-field images arise from the constructive interference between the tip-launched and end-reflected plasmon waves. The near-field response along the nanotube is fitted to a damped oscillator form $e^{-2\pi x/(Q\lambda_p)}\sin\left((4\pi x)/\lambda_p\right)$, with x measured from the nanotube end. We then extract both the plasmon wavelength λ_p and the quality factor Q. At different gate voltages, we observe that λ_p and Q remain largely unchanged at 90 nm and 22, respectively. At an excitation frequency f of ~28.3 THz, the plasmon velocity can be calculated as $v_p = \lambda_p f$, or ~2.5×10^6 m s^{-1}. The interaction type and strength between electrons in SWNTs is characterized by the Luttinger liquid parameter g. We find $g = v_0/v_p$ or ~0.31, which indicates the presence of strong electron–electron repulsion in metallic SWNTs. In marked comparison, near-field optical responses in the nanotubes labelled S1 and S2 in Fig. 2a depend sensitively on gate voltages. These two nanotubes correspond to semiconducting SWNTs with a hyperbolic dispersion. When the carrier density is near charge neutrality (Fig. 2c), the near-field response is dramatically depleted and we observe a weak contrast against the substrate. At substantial doping, well-defined plasmon features emerge and evolve with the gate voltage in both semiconducting nanotubes. The distinctly different plasmon behaviours highlight the critical role of nonlinear band dispersion in semiconducting SWNTs, which goes beyond the conventional linear Luttinger liquid paradigm in metallic SWNTs.

Next we examine comprehensively the plasmon behaviours in semiconducting nanotubes and their dependence on carrier density. Figure 3a shows the topography of a semiconducting nanotube, and the inset blue curve shows the height profile along the white dashed line across the nanotube. The diameter is determined to be 2 nm from the height profile and the nanotube thus has a band gap of ~ 0.37 eV. The near-field responses of the nanotube at different gate voltages from −20 to 24 V are presented in Fig. 3b–l. The near-field response evolves in a systematic manner, which is consistent with the semiconducting SWNTs in Fig. 2. At $V_g = -5$ V (Fig. 3e), the response is almost completely depleted, which corresponds to the charge neutral point. When carrier density is increased to either the hole-doped side (Fig. 3b–d) or the electron-doped side (Fig. 3f–l), there is an increase in the near-field optical response, and well-defined plasmons emerge at substantial doping as manifested by the oscillation peaks near the nanotube end. Line profiles along the dashed line in Fig. 3b reveal how the plasmon wave is damped as it propagates (Supplementary Fig. 2b). By fitting the line profiles with a damped oscillator form, we can extract both the plasmon wavelength and quality factor as a function of gate voltage. The results are summarized in Fig. 4b,d (ref. [27]). It is evident that plasmons in the semiconducting SWNT can be continuously tuned by means of electrostatic gating. With increasing gate voltage and thus higher Fermi level, the plasmon wavelength increases and the quality factor also shows concomitant growth. Below a critical carrier density indicated by the dashed line in Fig. 4b, the damping is too large to support well-defined plasmons.

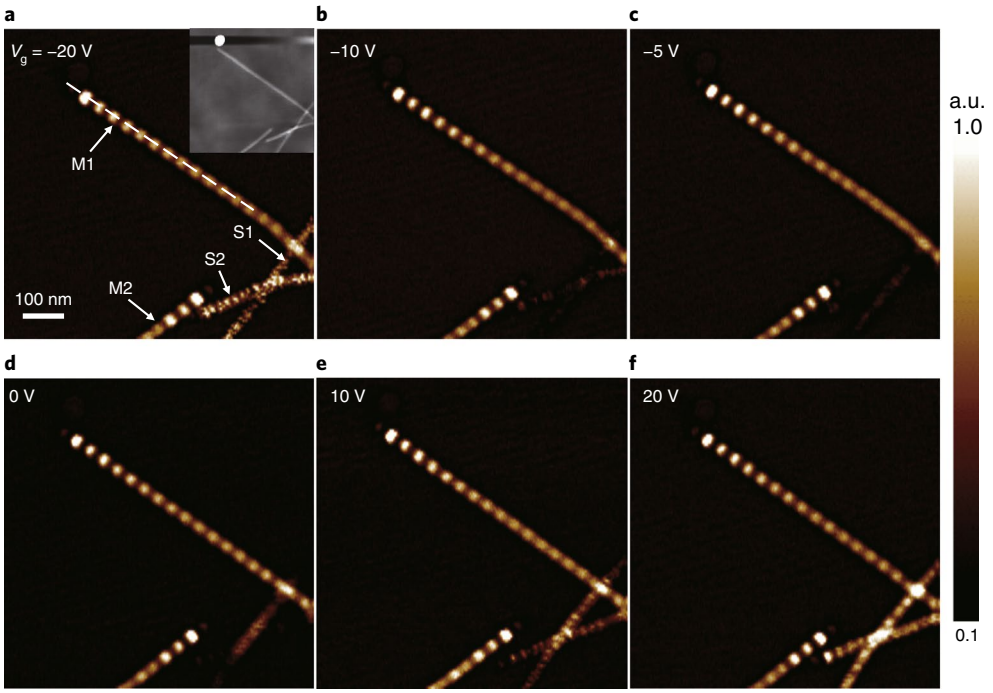

Fig. 2 | Infrared nano-imaging of metallic and semiconducting SWNTs at different gate voltages. a–f, From **a** to **f**, the gate voltage is varied from −20 to 20 V. The carrier density changes from hole doping to charge neutrality and then to electron doping. The plasmon features in the metallic nanotubes labelled M1 and M2 in **a** are largely unchanged. In marked comparison, the near-field optical responses in the semiconducting nanotubes, labelled S1 and S2 in **a**, depend sensitively on gate voltages. The line profiles along the nanotube (indicated by the white dashed line in **a**) reveal how the plasmon wave in metallic nanotube M1 gets damped as it propagates. The profiles for different gate voltages (**a–f**) are plotted in Supplementary Fig. 2a. The inset in **a** shows the topography recorded simultaneously with the near-field images. The colour scale shows the infrared response.

As observed in Fig. 2, the gate-independent plasmon behaviour in metallic SWNTs is well described by linear Luttinger liquid theory[13,23,24]. For an individual suspended carbon nanotube of radius R screened by a concentric metal shell of radius R_s, the linear Luttinger liquid theory predicts the Luttinger liquid interaction parameter g to be

$$\frac{1}{g} = \frac{v_p}{v_F} = \sqrt{1 + \frac{8e^2}{4\pi\varepsilon_{eff}\pi\hbar v_F}\ln\left(\frac{R_s}{R}\right)}$$

where v_p is the velocity of the collective charge mode, that is plasmon velocity; v_F is the Fermi velocity; and ε_{eff} is the effective dielectric constant due to substrate screening. This parameter g is only a function of Fermi velocity and the ratio R_s/R for a nanotube under a given dielectric environment. The plasmon wavelength λ_p for a given frequency f is related to g as $\lambda_p = v_p/f = v_F/(gf)$. Because the Fermi velocity is a constant in metallic SWNTs, all the Luttinger liquid phenomena related to g, including the plasmon excitations, will be independent of carrier density.

By contrast, the gate-tunable plasmon wavelength in semiconducting nanotubes stems from the hyperbolic band dispersion, where the Fermi velocity v_F depends on carrier density. As illustrated in Fig. 4a, the Fermi velocity indicated by the slope of the black tangent line increases with higher Fermi energy. Due to the dominant strong repulsive interaction in SWNTs, plasmon velocity v_p is approximately proportional to $\sqrt{v_F}$, and the plasmon wavelength in semiconducting nanotubes with band gap E_g depend on the Fermi wavevector k_F as follows:

$$\lambda_p = \lambda_{p0}\sqrt{\frac{v_F}{v_0}} = \lambda_{p0}\sqrt{\frac{\hbar v_0 k_F}{\sqrt{(E_g/2)^2 + (\hbar v_0 k_F)^2}}}$$

where λ_{p0} and v_0 are the plasmon wavelength and Fermi velocity, respectively, in metallic nanotubes for a given frequency. Thus one can expect that the plasmon wavelength in semiconducting nanotubes will increase and progressively approach that in metallic ones with larger k_F. The experimentally observed tunable plasmon wavelength at substantially high doping in semiconducting nanotubes (Fig. 3h–l) is well reproduced by the theoretical model (Fig. 4b). In this fitting we have used $k_F = \frac{\pi}{4}n = \frac{\pi}{4}\beta C_g|V_g - V_{cnp}|$, where n is the carrier density, C_g is the geometric capacitance and β is a fitting parameter and indicates the overall gate efficiency.

Apart from the tunable plasmon wavelength, the quality factor also depends sensitively on gate voltage as shown in Fig. 4d. The tunable damping behaviours are reminiscent of those in graphene plasmons, which can be captured by Landau damping within the random-phase approximation (RPA). The gate-dependent plasmon damping behaviour in semiconducting nanotubes shown in Fig. 3h–l, however, cannot be explained by this simple picture. No interband damping can exist in a semiconducting nanotube due to its large band gap (~0.37 eV) compared with the excitation energy (~0.10 eV). It has also been shown that 1D plasmons will not decay to a single electron–hole pair through intraband scattering within the RPA[28]. As illustrated in Fig. 4e, within the RPA theory, the plasmon excitation, $\omega(q)$, indicated by the orange dashed line, always lies outside the electron–hole continuum indicated by the blue shaded area, and thus is free from Landau damping.

We can rule out defect and/or acoustic phonon scattering as a main contribution to the plasmon damping by comparing the infrared near-field nanoscopy results with the electronic transport in semiconducting SWNTs with the same diameter and growth conditions. Figure 4c displays the gate-dependent d.c. transport data[27] of a representative SWNT with a diameter of 2 nm and a channel

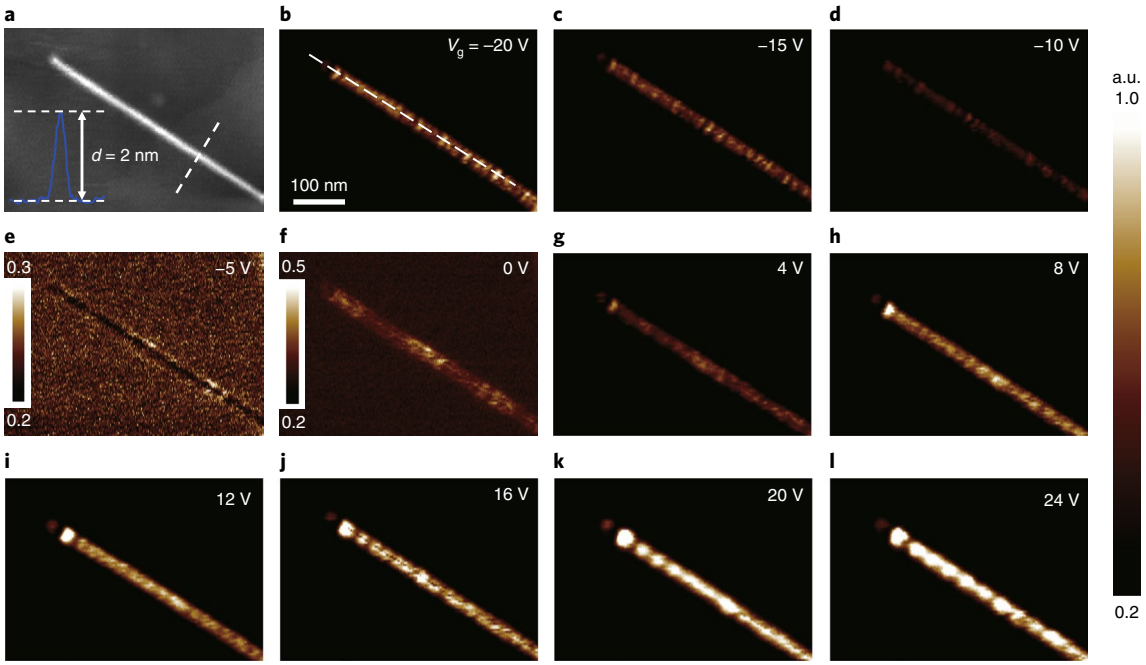

Fig. 3 | Gate-tunable plasmons in semiconducting SWNTs. a, AFM topography of a semiconducting nanotube. The inset blue curve is the height profile along the white dashed line across the nanotube, and the diameter is determined to be 2 nm from the profile. **b**–**l**, Near-field responses of the semiconducting nanotube at different gate voltages from −20 to 24 V. Plasmons in the semiconducting SWNT can be continuously tuned by means of electrostatic gating. With increasing gate voltage and thus higher Fermi level, the plasmon wavelength increases and the quality factor also shows concomitant growth. The figures share the same colour scale (to give a direct comparison of the infrared responses at different gate voltages) except for **e** and **f**, where the scales shown in the insets are intentionally made smaller to offer better contrast between the nanotube and the substrate. The line profiles along the nanotube (indicated by the white dashed line in **b**) reveal how the plasmon wave in the semiconducting nanotube gets damped as it propagates. The profiles for different gate voltages (**h**–**i**) are plotted in Supplementary Fig. 2b.

length L of 4 μm by recording the source drain current I_{sd} for different gate voltages at a bias of V_{sd}=6 mV. The optical image of the SWNT device is shown in the inset. From the measured gate-dependent 1D channel resistance R, we can estimate the mean free path $L_m = \frac{L}{R4e^2/h-1}$ (h is Planck's constant) and scattering time $\tau = L_m/v_F$ at different gate voltages. The scattering of electrons close to the Fermi surface, which dominates the electronic transport, is mainly due to defects and acoustic phonons in semiconducting SWNTs at room temperature[29,30]. We obtain an electron scattering time longer than 300 fs, corresponding to a scattering rate of ~3 ps^{-1}, for a carrier density approaching the saturation region for the semiconducting nanotube, which is consistent with previous findings in electronic transport studies of high-quality semiconducting SWNTs[30,31]. This electron scattering rate is over an order of magnitude smaller than the observed plasmon damping rate. If we assume plasmon damping to have similar origins as the d.c. transport (that is, dominated by defect and acoustic phonon scattering), the quality factor determined by $\omega\tau$ will be very high and exhibit a completely different gate dependence (red line and right scale in Fig. 4d) compared with the plasmon behaviour. Our experimental data cannot be accounted for by the emission of optical phonons either, because the optical phonon scattering should have a weaker dependence on the doping concentration.

The observed, unusual gate-dependent plasmon damping in semiconducting nanotubes, on the other hand, can be naturally understood as a consequence of the strong plasmon–plasmon coupling in a nonlinear Luttinger liquid: in metallic nanotubes with perfect linear dispersion, the plasmon excitations are free, long-lived bosons without an intrinsic relaxation mechanism within the linear Luttinger liquid theory paradigm. The nonlinear band dispersion in semiconducting nanotubes, however, can enable extremely strong coupling between different plasmon modes because they all propagate at the same speed. As a result, a high-energy plasmon can efficiently decay into multiple low-energy plasmons in semiconducting nanotubes.

A universal description of the dynamic response function in a nonlinear Luttinger liquid has been theorized previously[17,21]. The dynamic excitation of plasmons in a 1D system is determined by the dynamic structure factor (DSF). For a linear Luttinger liquid as in metallic SWNTs, the DSF takes the form $S(q,\omega) = 2g|q|\delta(\omega - v_p q)$. This suggests that the plasmon mode features a linear dispersion $\omega(q) = v_p q$ indicated by the dashed orange line in Fig. 4f and is free of intrinsic relaxation. For a nonlinear Luttinger liquid as in gated semiconducting SWNTs, the DSF is given by

$$S(q,\omega) = 2\frac{\tilde{m}g}{|q|}\theta\left(\frac{q^2}{2\tilde{m}} - |\omega - v_p q|\right)$$

with an effective mass $\tilde{m}$. The effective mass $\tilde{m}$ depends on electron–electron interactions, and it can be expressed as $\frac{1}{\tilde{m}} = \frac{v_p}{2g}\frac{\partial}{\partial E_F}(v_p\sqrt{g})$. θ is the Heaviside step function. The plasmon mode is thus not an exact eigenstate but is broadened with upper and lower bounds, $\omega_\pm(q) = v_p q \pm q^2/2\tilde{m}$, as indicated by the red lines in Fig. 4f. The width of the broadening is $\delta\omega(q) = q^2/\tilde{m}$. For a given frequency, a set of plamson modes with different momenta can be excited in the shaded grey area where DSF differs from zero. This broadening reflects the finite lifetime and damping of the plasmons. As the Fermi energy E_F increases compared with the excitation energy ω, the broadening becomes less severe and well-defined plasmons begin to emerge, in agreement with experimental observations.

This dissipation reflected in the broadening of the DSF can be further quantitatively characterized as $\delta\omega/\omega = \omega/\tilde{m}v_p^2$.

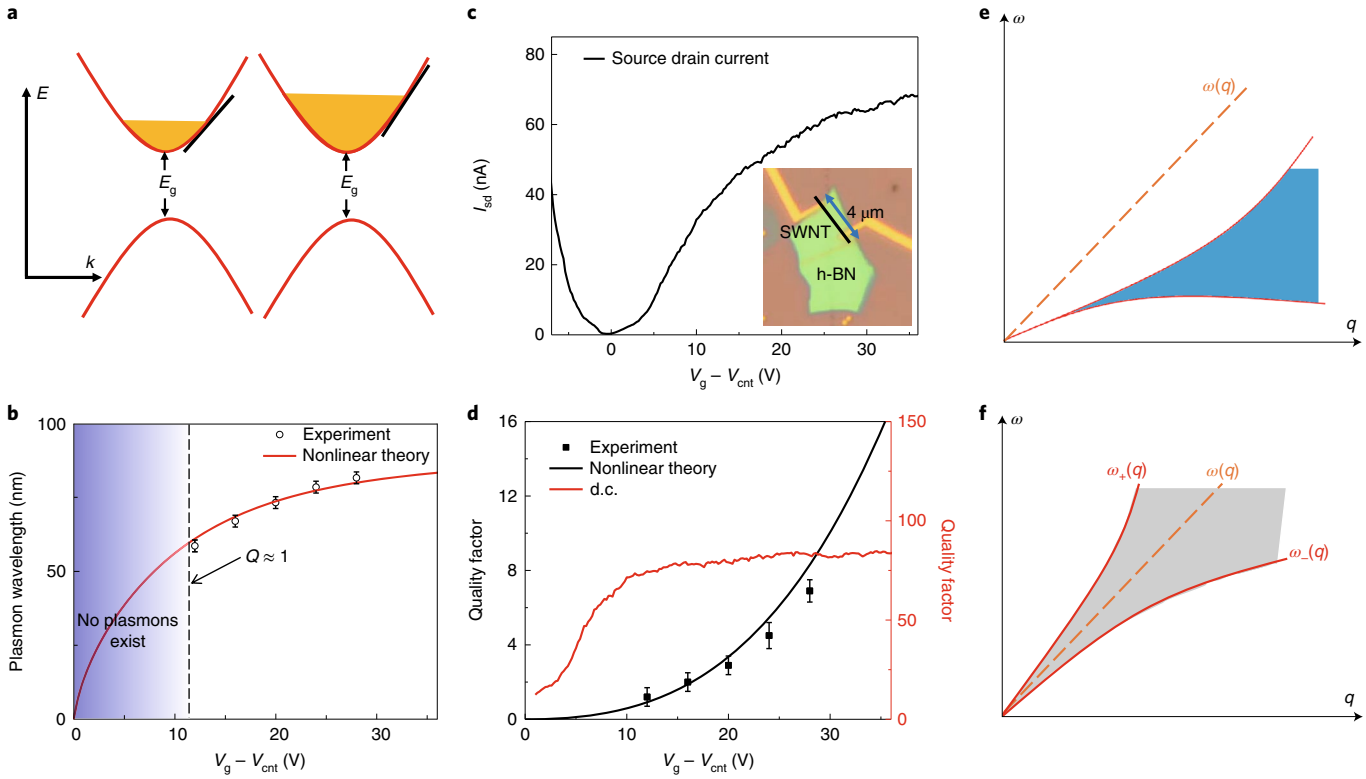

Fig. 4 | Nonlinear Luttinger liquid model and comparison with experimental results. a, Illustrative hyperbolic E–k dispersion (red curve) and Fermi energy (filled yellow region) of a semiconducting SWNT with a band gap E_g. The Fermi velocity indicated by the slope of the black tangent line increases with higher Fermi energy. **b**, The dependence of the plasmon wavelength on gate voltage agrees well with the theoretical model. Below a critical doping indicated by the dashed line (shaded blue area), the plasmon quality factor Q is not large enough for well-defined plasmons to exist. **c**, A curve showing the source drain current versus gate voltage (I_{sd}–V_g) for a 2-nm-diameter semiconducting nanotube at a bias $V_{sd} = 6$ mV. The inset is an optical image of the device with a channel length of ~4 μm. **d**, The nonlinear theory (black line) can reproduce the experimental dependence of the quality factor on the gate voltage (black symbols) well. On the other hand, the plasmon quality factor will be very high and exhibit a completely different gate dependence (red line and right scale) if the damping rate is the same as the electron scattering rate inferred from d.c. transport measurements. **e**, Illustration of the plasmon dispersion within the RPA. Here the plasmon excitation, $\omega(q)$, indicated by the orange dashed line, always lies outside the electron–hole continuum indicated by the blue shaded area and is thus free from Landau damping. **f**, Illustrative diagram of DSF from the universal nonlinear Luttinger liquid theory. In a nonlinear Luttinger liquid, the plasmon mode indicated by the grey shaded area is not an exact eigenstate $\omega(q) = v_p q$ but is broadened with an upper and lower bound, $\omega_\pm(q) = v_p q \pm q^2/2\tilde{m}$. Error bars in **b** and **d** indicate a 95% confidence interval determined from the curve fitting of the line profiles along the nanotube in Fig. 3 with a damped oscillator form.

In semiconducting nanotubes with a hyperbolic dispersion, this broadening depends on the Fermi wavevector k_F as

$$\frac{\delta\omega}{\omega} = \frac{3\sqrt{3}}{8}\left(\frac{\sqrt{(E_g/2)^2+(\hbar v_0 k_F)^2}}{\hbar v_0 k_F}\right)^{\frac{5}{4}} \frac{(E_g/2)^2}{(E_g/2)^2+(\hbar v_0 k_F)^2}\frac{\omega}{v_0 k_F}$$

The plasmon quality factor determined by this nonlinear dispersion can be described as $\omega/\delta\omega$, and its dependence on gate voltage is depicted in Fig. 4d. The nonlinear theory (black line) can reproduce the experimental results (black symbols) well. With increasing carrier density and Fermi energy, the band structure gradually approaches a linear dispersion. This decrease in the nonlinearity of dispersion leads to the increase of plasmon lifetime and a higher quality factor observed in the experiments. The small discrepancy might indicate that other damping mechanisms also play a role, but nevertheless are not dominant in our experiment. We conclude that in doped semiconducting nanotubes with a hyperbolic dispersion, at the high-energy regime where the excitation energy is comparable to the Fermi energy, the system should be described as a nonlinear Luttinger liquid and the plasmon damping mechanism is dominated intrinsically by the nonzero curvature of the band dispersion. Note that if we probe at the low-energy regime where the excitation energy is much smaller than the Fermi energy, $\delta\omega/\omega$ will be vanishingly small, and the system will reproduce the linear Luttinger liquid regime. The intriguing gate-dependent nonlinear Luttinger liquid plasmon behaviours offer the alluring capability of active electrical switching and tuning of plasmons in semiconducting nanotubes. The highly confined and tunable plasmons and their compatibility with FET devices hold great promise for integrated nanophotonic applications[32,33].

Online content

Any methods, additional references, Nature Research reporting summaries, source data, extended data, supplementary information, acknowledgements, peer review information; details of author contributions and competing interests; and statements of data and code availability are available at https://doi.org/10.1038/s41563-020-0652-5.

Received: 16 October 2019; Accepted: 2 March 2020;
Published online: 30 March 2020

References

1. Tomonaga, S. Remarks on Bloch's method of sound waves applied to many-fermion problems. *Prog. Theor. Phys.* **5**, 544–569 (1950).
2. Luttinger, J. M. An exactly soluble model of a many-fermion system. *J. Math. Phys.* **4**, 1154–1162 (1963).
3. Haldane, F. D. M. 'Luttinger liquid theory' of one-dimensional quantum fluids. I. Properties of the Luttinger model and their extension to the general 1D interacting spinless Fermi gas. *J. Phys. C Solid State* **14**, 2585–2609 (1981).
4. Giamarchi, T. *Quantum Physics in One Dimension* Ch. 3 (Oxford Univ. Press, 2004).
5. Giuliani, G. & Vignale, G. *Quantum Theory of the Electron Liquid* Ch. 9 (Cambridge Univ. Press, 2005).
6. Deshpande, V. V., Bockrath, M., Glazman, L. I. & Yacoby, A. Electron liquids and solids in one dimension. *Nature* **464**, 209–216 (2010).
7. Voit, J. One-dimensional Fermi liquids. *Rep. Prog. Phys.* **58**, 977–1116 (1995).
8. Bockrath, M. et al. Luttinger-liquid behaviour in carbon nanotubes. *Nature* **397**, 598–601 (1999).
9. Yao, Z., Postma, H. W. C., Balents, L. & Dekker, C. Carbon nanotube intramolecular junctions. *Nature* **402**, 273–276 (1999).
10. Ishii, H. et al. Direct observation of Tomonaga–Luttinger-liquid state in carbon nanotubes at low temperatures. *Nature* **426**, 540–544 (2003).
11. Jompol, Y. et al. Probing spin-charge separation in a Tomonaga-Luttinger liquid. *Science* **325**, 597–601 (2009).
12. Zhao, S. et al. Correlation of electron tunneling and plasmon propagation in a Luttinger liquid. *Phys. Rev. Lett.* **121**, 047702 (2018).
13. Kane, C., Balents, L. & Fisher, M. P. A. Coulomb interactions and mesoscopic effects in carbon nanotubes. *Phys. Rev. Lett.* **79**, 5086–5089 (1997).
14. Egger, R. & Gogolin, A. O. Effective low-energy theory for correlated carbon nanotubes. *Phys. Rev. Lett.* **79**, 5082–5085 (1997).
15. Williams, P. F. & Bloch, A. N. Self-consistent dielectric response of a quasi-one-dimensional metal at high frequencies. *Phys. Rev. B* **10**, 1097–1108 (1974).
16. Pustilnik, M., Khodas, M., Kamenev, A. & Glazman, L. I. Dynamic response of one-dimensional interacting fermions. *Phys. Rev. Lett.* **96**, 196405 (2006).
17. Imambekov, A. & Glazman, L. I. Universal theory of nonlinear Luttinger liquids. *Science* **323**, 228–231 (2009).
18. Imambekov, A. & Glazman, L. I. Phenomenology of one-dimensional quantum liquids beyond the low-energy limit. *Phys. Rev. Lett.* **102**, 126405 (2009).
19. Barak, G. et al. Interacting electrons in one dimension beyond the Luttinger-liquid limit. *Nat. Phys.* **6**, 489–493 (2010).
20. Schmidt, T. L., Imambekov, A. & Glazman, L. I. Spin-charge separation in one-dimensional fermion systems beyond Luttinger liquid theory. *Phys. Rev. B* **82**, 245104 (2010).
21. Imambekov, A., Schmidt, T. L. & Glazman, L. I. One-dimensional quantum liquids: beyond the Luttinger liquid paradigm. *Rev. Mod. Phys.* **84**, 1253–1306 (2012).
22. Jin, Y. et al. Momentum-dependent power law measured in an interacting quantum wire beyond the Luttinger limit. *Nat. Commun.* **10**, 2821 (2019).
23. Wang, S. et al. Logarithm diameter scaling and carrier density independence of one-dimensional Luttinger liquid plasmon. *Nano Lett.* **19**, 2360–2365 (2019).
24. Shi, Z. et al. Observation of a Luttinger-liquid plasmon in metallic single-walled carbon nanotubes. *Nat. Photonics* **9**, 515–519 (2015).
25. Liu, M., Sternbach, A. J. & Basov, D. N. Nanoscale electrodynamics of strongly correlated quantum materials. *Rep. Prog. Phys.* **80**, 014501 (2016).
26. Saito, R., Dresselhaus, G. & Dresselhaus, M. S. *Physical Properties of Carbon Nanotubes* Ch. 4 (Imperial College Press, 1998).
27. Wang, S. et al. Nonlinear Luttinger liquid plasmons in semiconducting single walled carbon nanotubes. *Figshare* https://doi.org/10.6084/m9.figshare.11900307.v2 (2020).
28. das Sarma, S. & Hwang, E. H. Dynamical response of a one-dimensional quantum-wire electron system. *Phys. Rev. B* **54**, 1936–1946 (1996).
29. Jorio, A., Dresselhaus, G., & Dresselhaus, M. S. *Carbon Nanotubes: Advanced Topics in the Synthesis, Structure, Properties and Applications* Ch. 15 (Springer, 2008).
30. Zhou, X., Park, J.-Y., Huang, S., Liu, J. & McEuen, P. L. Band structure, phonon scattering, and the performance limit of single-walled carbon nanotube transistors. *Phys. Rev. Lett.* **95**, 146805 (2005).
31. Purewal, M. S. et al. Scaling of resistance and electron mean free path of single-walled carbon nanotubes. *Phys. Rev. Lett.* **98**, 186808 (2007).
32. He, X. et al. Carbon nanotubes as emerging quantum-light sources. *Nat. Mater.* **17**, 663–670 (2018).
33. Ozbay, E. Plasmonics: merging photonics and electronics at nanoscale dimensions. *Science* **311**, 189–193 (2006).

Methods

Carbon nanotube growth and device fabrications. Ferritin solution (0.1 mmol l^{-1}) is drop-casted onto SiO_2/Si substrates (SiO_2, 285 nm). The substrates are incubated at room temperature for 10 min. The substrates are then rinsed with isopropyl alcohol and are subsequently blow-dried. The substrates are annealed in air at 900 °C for 30 min to convert ferritin to Fe_2O_3 nanoparticles. Then h-BN flakes are mechanically exfoliated onto the SiO_2/Si substrates with Fe_2O_3 nanoparticles. High-quality SWNTs are then directly grown on the substrates by CVD. We use an ambient-pressure CVD system equipped with a one-inch quartz tube. The system is first purged with hydrogen gas for 10 min to get rid of the air. After that, the temperature is raised to 900 °C in 15 min under 300 sccm of hydrogen flow. When the temperature reaches 900 °C, 110 sccm of argon is introduced through a bubbler with ethanol, which works as the carbon precursor, while 300 sccm of hydrogen flow is maintained to reduce iron compound nanoparticles to iron nanoparticles, which act as catalysts for SWNT growth. The temperature is kept at 900 °C for 15 min, followed by naturally cooling to room temperature under a hydrogen flow of 300 sccm. Electrical contacts on the SWNTs are then fabricated using standard e-beam lithography or shadow masks. For individual nanotube transport measurement, SWNTs on SiO_2 are thoroughly eliminated by an oxygen plasma, with the nanotube between the electrodes left for transport measurement. Shadow masks are used to define one contact for back gating to avoid polymer contamination and to keep the nanotubes ultraclean for gate-controlled infrared nano-imaging. E-beam lithography is used to define electrodes for electronic transport measurements.

Infrared nano-imaging of carbon nanotube plasmons. The scattering-type SNOM for this work is based on a tapping mode AFM (Bruker Innova). For infrared nano-imaging, a CO_2 laser with wavelength 10.6 μm is focused onto the apex of a gold-coated AFM tip (Nanoandmore) with a radius of tip apex ~20 nm. The tapping frequency (Ω) and amplitude of the tip are ~240 kHz and ~80 nm, respectively. The backscattered signal from the tip apex carries local optical information of the sample and is captured by a MCT detector (Kolmar Technologies KLD-0.1-J1/11/DC) in the far field. The detector signal is demodulated at a frequency of 3Ω by a lock-in amplifier (Zurich Instruments HF2LI) to suppress the background scattering from the tip shaft and sample. By a raster scanning of the sample, near-field images are obtained simultaneously with the topography.

Data availability

The numerical data represented in Fig. 4b–d are provided with the paper as source data. All other data that support results in this Article are available from the corresponding author upon reasonable request.

Code availability

Matlab codes for nonlinear theory calculation are available from the corresponding author upon reasonable request.

Acknowledgements

We thank N. Yao, R. Vasseur, J. Kang and H. B. Balch for helpful discussions. This work was mainly supported by the Director, Office of Science, Office of Basic Energy Sciences, Materials Sciences and Engineering Division of the US Department of Energy under contract no. DE-AC02-05-CH11231 (sp2-Bonded Materials Program KC2207). The device fabrication and electrical measurement were supported by the Office of Naval Research (MURI award N00014-16-1-2921). The data analysis was supported by the NSF award 1808635. Z.S. acknowledges support from the National Natural Science Foundation of China (11774224 and 11574204). F. Wu, Z.Z. and C.Z. acknowledge the National Science Foundation for financial support under grant no. 769K521. K.W. and T.T. acknowledge support from the Elemental Strategy Initiative conducted by the MEXT, Japan and the CREST (JPMJCR15F3), JST.

Author contributions

F. Wang, S.W. and Z.S. conceived the project and designed the experiment. F. Wang and C.Z. supervised the project. S.W. fabricated the devices and performed the infrared nano-imaging measurements. S.Z. and S.W. fabricated the devices for the transport measurements and carried out the electrical measurements. F. Wu and Z.Z. under the supervision of C.Z. grew the SWNT samples and performed scanning electron microscopy. Z.S., L.J. and A.Z. assisted in device fabrication. K.W. and T.T. provided the h-BN crystals. S.W. and F. Wang analysed the data. All authors contributed to the writing of the manuscript.

Competing interests

The authors declare no competing interests.

Additional information

Supplementary information is available for this paper at https://doi.org/10.1038/s41563-020-0652-5.

Correspondence and requests for materials should be addressed to F.W.